Article

Impacts of leaf traits on vegetation optical properties in Earth system modeling

Yujie Wang [1,2,6] ✉, Renato K. Braghiere [2,3,6], Woodward W. Fischer[2], Yitong Yao[2], Zhaoyi Shen [2], Tapio Schneider [2], A. Anthony Bloom[3], David Schimel[3], Holly Croft[4], Alexander J. Winkler [5], Markus Reichstein [5] & Christian Frankenberg [2,3]

Quantifying surface energy and carbon budgets is essential for projecting Earth's climate. Earth System Models (ESMs) typically simulate land surface processes based on plant functional types (PFTs), neglecting the diversity of plant functional traits or characteristics (PFCs; e.g., chlorophyll content and leaf mass per area). Here, we demonstrate substantial differences in modeled leaf optical properties (LOP) and surface albedo between traditional PFT-based and PFC-based approaches, particularly in tropical and boreal forests. We configure the canopy radiative transfer scheme in the Community Earth System Model using PFC-based LOP. This new configuration produces lower shortwave surface albedo in the tropics but higher albedo in boreal regions (>5 W m^{-2} radiative flux differences), and a weaker tropical but stronger boreal carbon sink. Through land-atmosphere coupling, the PFC-based configuration further alters atmospheric processes, leading to different temperature, cloud cover, and precipitation patterns. Our findings highlight the need to move beyond traditional PFT-based approaches in ESMs.

Global average surface temperature has increased by about 1.5 °C in 2024 compared to 1850–1900. This additional warming has driven elevated regional and seasonal temperature extremes[1,2], reduced snow cover and sea ice[3], and intensified heavy rainfall[2,4]. The unprecedented global climate change also poses increasing threats to plants, animals, and human societies[3,5], with widespread impacts on biodiversity, food security, and human health. To meet the 2 °C goal set in the Paris Agreement, countries must take drastic climate actions to reduce greenhouse gas emissions and increase carbon capture[6,7]. Terrestrial plants affect surface albedo[8], sequester about 3.3 ± 0.8 Gt C per year during the 2013–2022 decade (about 31% of total CO_2 emissions)[9], and recycle moisture, contributing ~39 ± 10% to precipitation via transpiration[10]. Thus, accurately modeling vegetation dynamics is key for quantifying Earth's surface fluxes of energy, water, and carbon, projecting atmospheric CO_2 concentration, and assessing nature-based climate solutions (such as reforestation and soil carbon capture).

In recent years, much effort has been devoted to implementing and improving the global carbon cycle in ESMs[11–13]. Land surface models (LSMs) in ESMs have also improved their process representations of the vegetation energy balance, including the incorporation of multilayer canopy and canopy heterogeneity[14–18]. Despite significant advances, systematic biases persist in the modeled surface energy balance[19,20], potentially leading to biases in future climate projections. These biases may arise from the following issues: (1) Radiative transfer (RT) schemes are often oversimplified limiting their ability to capture the spectrally resolved optical properties of plants and incoming radiation sources[20,21]; (2) Key coupled processes remain underrepresented, such as the impact of leaf water content (LWC) dynamics on leaf reflectance and transmittance[22–24] and leaf angles; (3) The Plant

[1]School of Earth and Space Sciences, University of Science and Technology of China, Hefei 230026 Anhui, China. [2]Division of Geological and Planetary Sciences, California Institute of Technology, Pasadena 91125 CA, USA. [3]Jet Propulsion Laboratory, California Institute of Technology, Pasadena 91109 CA, USA. [4]School of Biosciences, University of Sheffield, Sheffield S10 2TN, Germany. [5]Max-Planck-Institute for Biogeochemistry, Jena 07745, Germany. [6]These authors contributed equally: Yujie Wang, Renato K. Braghiere. ✉ e-mail: wyujie@ustc.edu.cn

Functional Type (PFT) paradigm commonly employed to represent plant diversity has limitations in capturing important variations in vegetation traits or characteristics within PFTs[12,25,26], such as variations in leaf optical and other ecophysiological properties. The reliance on PFTs in LSMs reflects a historical legacy from their initial development in the 1980s, when observational data and computational resources were limited[27]. This legacy poses significant challenges to fully restructuring LSMs around trait-based approaches.

Over the past 40 years, great advances have been made in leaf and canopy RT models, permitting more sophisticated representations of radiation profiles across hyperspectral wavelengths in a vertically resolved canopy[15,17,21,22,28–30]. Moreover, the value of implementing plant physiological processes into vegetation modeling, such as the importance of plant hydraulics in regulating stomatal responses to environmental conditions, has been increasingly recognized[31–35]. A growing number of global datasets of Plant Functional Characteristics (PFCs) derived from global databases[36–39] and remote sensing observations[40–42] further enabled a shift from PFT-based (categorical) to PFC-based (continuous) modeling[43]. However, incorporating these advances into ESMs faces grand challenges given the complex nature of ESMs and the lack of data needed to configure and calibrate them[44,45]. For example, complex RT models require substantial computational resources; limited trait data is available to feed process- and trait-based vegetation models (e.g., certain plant hydraulic traits are laborious to measure).

Due to limited knowledge of key leaf and canopy parameters and computational efficiency, canopy RT schemes in LSMs often simulate the shortwave radiation scattering and absorption with two broad bands: one covering the visible light that promotes photosynthesis (also known as photosynthetically active radiation, PAR; 400–700 nm) and another covering the near-infrared radiation (NIR; 700–2500 nm)[19,46–53]. Recently, it has been proposed that a portion of the NIR spectrum between 700–750 nm be included as PAR, given that chlorophyll in the light-harvest complexes can also absorb far-red photons for photosynthesis[21,54]. Leaf reflectance (ρ) and transmittance

(τ) within the two broad bands are typically predefined to be constants based on PFT (Supplementary Note 1). Although the PFT-based look-up table approach can qualitatively represent general variations among vegetation groups such as trees and grasses, it does not accurately represent the spatial and temporal diversity in associated plant traits[25,55]. For example, higher leaf chlorophyll content (CHL) reduces both reflectance and transmittance in the PAR range; higher leaf mass per area (LMA) decreases reflectance and transmittance primarily in the NIR range (Fig. 1a). However, in current LSMs, the broadband leaf ρ and τ values are prescribed from the PFT-based look-up tables, irrespective of variation in CHL, LMA, or other traits[46–53]. Promisingly, recent advances in RT modeling, remote sensing technologies, and plant trait databases have allowed the implementation of more complex and process-based schemes in LSMs and ESMs due to the increasing amount of observations that can be used to understand, initialize, and calibrate vegetation processes[29,39,42,43,56].

In this study, we aim to reconcile (a) the requirement of computational efficiency by ESMs and (b) the needs of advancing canopy RT modeling, coupling vegetation processes, and representing vegetation biodiversity. We propose to use a trait- or PFC-based approach along with spatially resolved leaf optical properties (LOP), instead of the PFT-based approach with predefined LOP per PFT. First, we derived global-scale monthly hyperspectral LOP based on CHL[42] and LMA[37] using the next-generation LSM developed within the Climate Modeling Alliance −CliMA Land[17,21], which supports hyperspectral RT scheme and enables tight process-trait coupling. We then computed the monthly mean broadband values (PAR and NIR) from the hyperspectral LOP. Second, we used the annual mean ρ and τ per grid cell to supersede the PFT-based look-up table values in the Community Land Model (CLM; version 5), the land component of the Community Earth System Model (CESM; version 2)[52,57]. Third, we performed simulations with CESM at different climate scenarios: two land-atmosphere coupled simulations and three land-only (coupled historical 1950–2004, coupled Socio-economic Pathways [SSP] 585 2015–2099, uncoupled historical 1985–2019, and uncoupled SSP 245 and 585 from 2015 to 2104[58]; see
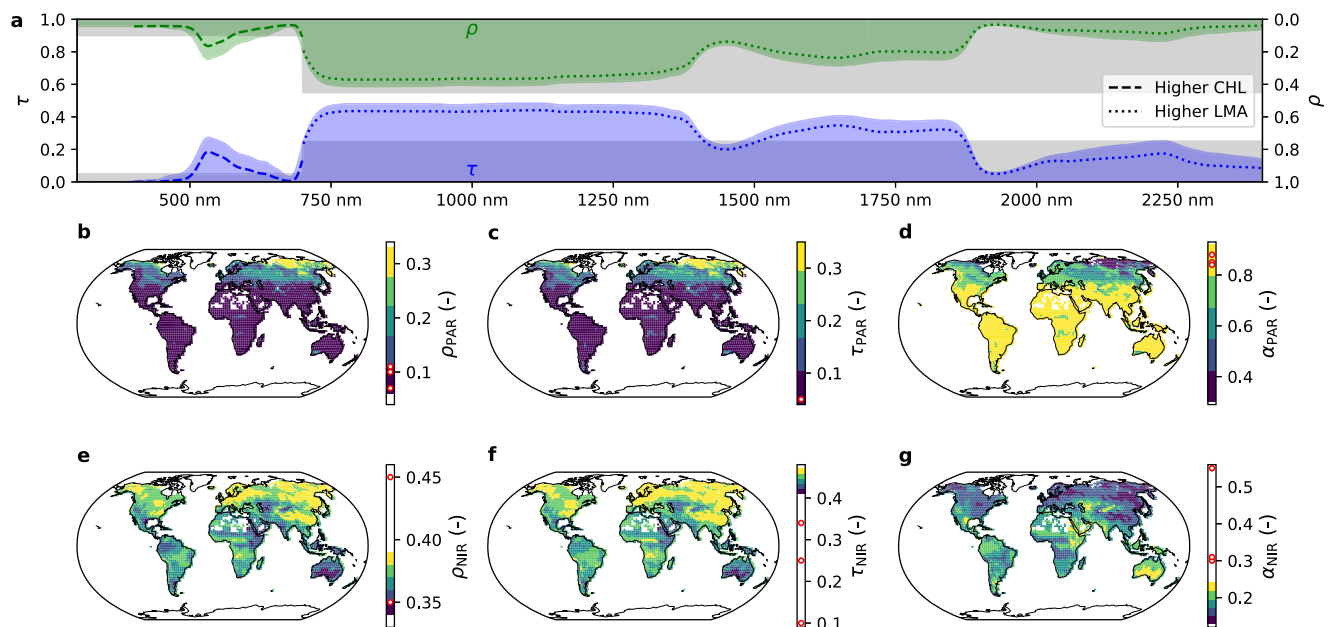

Fig. 1 | Leaf optical properties from CliMA Land based on global scale leaf chlorophyll content (CHL) and leaf mass per area (LMA). a Leaf hyperspectral reflectance (ρ, shaded green) and transmittance (τ, shaded blue) vary with CHL and LMA. The shaded gray regions plot the reflectance (ρ) and transmittance (τ) of a tropical broadleaf evergreen PFT. Dashed curves: leaf with higher CHL. Dotted curves: leaf with higher LMA. **b**–**g** Leaf broadband ρ, τ, and absorptance ($\alpha = 1 - \rho - \tau$) for photosynthetically active radiation (PAR, 400–700 nm) and near-infrared radiation (NIR, 700–2500 nm). The red open dots on the color bars plot values from the look-up table from the Community Earth System Model. Panels (**b**–**g**) made with Nature Earth. Free vector and raster map data @ naturalearthdata.com.
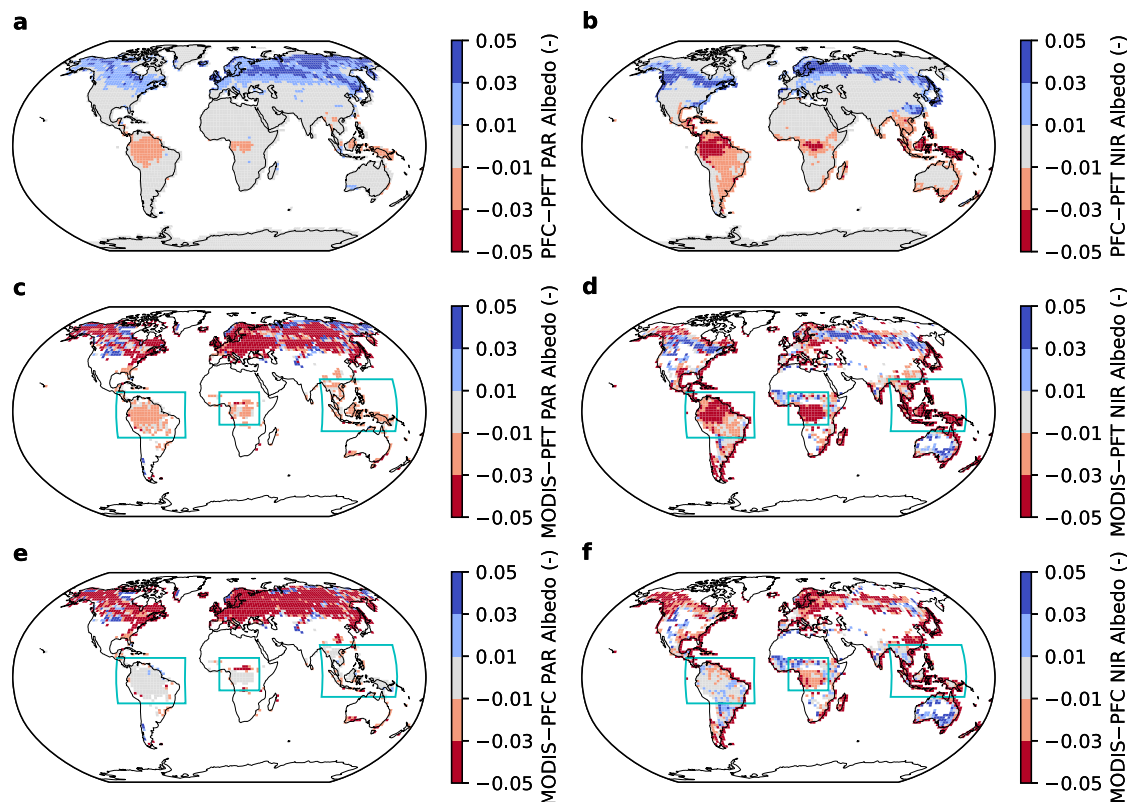
Fig. 2 | Spatial patterns of surface albedo differences between PFT- and PFC-based leaf optical property configurations. The simulations were made from 1985 to 2019 under the historical pathway (uncoupled). PAR: photosynthetically active radiation, NIR: near-infrared radiation, PFT: plant functional type, PFC plant functional characteristic. **a** PFT- and PFC-based surface PAR albedo difference. **b** PFT- and PFC-based surface NIR albedo difference. **c-d** Differences between MODIS and PFT-based surface PAR and NIR albedo in the regions where the

difference between PFT- and PFC-based albedo is ≥ 0.005. **e-f** Differences between MODIS and PFC-based surface PAR and NIR albedo in the regions where the difference between PFT- and PFC-based albedo is ≥0.005. The cyan rectangles mark the regions with potential improvements in the tropical rainforests. We excluded the regions with changes <0.005 for better visualization. Made with Nature Earth. Free vector and raster map data @ naturalearthdata.com.

Methods for more details). By comparing the CESM outputs using PFT- and PFC-based approaches, we assessed the impacts on the global surface energy budget, carbon cycle, and climate predictions.

Results

Leaf optical properties

The PFC-based (or trait-based) LOP derived from CliMA Land showed different patterns and ranges compared to the PFT-based look-up tables used in CESM (Fig. 1b–g). For example, annual mean ρ_{PAR} computed from CHL and LMA ranged from 0.06 to 0.32 globally while being set to 0.07, 0.10, and 0.11 in CLM depending on the PFT (Fig. 1b). Similarly, annual mean τ_{PAR} computed from CHL and LMA ranged from 0.04 to 0.35 while being set constant at 0.05 in CLM for all PFTs (Fig. 1c). The look-up table values in CESM matched the PFC-based annual mean only in tropical and temperate forests with high CHL[42] but showed much higher PAR absorption in boreal regions (Fig. 1d). Regarding NIR, the PFC-based ρ_{NIR} ranged from 0.34 to 0.39, while the look-up table values were 0.35 and 0.45, with the broadleaf PFTs (0.45) falling out of the modeled range (Fig. 1e; Supplementary Note 1). The PFC-based τ_{NIR} ranged from 0.41 to 0.47, consistently higher than the leaf reflectance settings of 0.10, 0.25, and 0.34 in CESM (Fig. 1f). Consequently, leaf-level NIR absorptance was consistently higher in the PFT-based setup.

Due to CHL seasonality[42], the PFC-based ρ_{PAR} and τ_{PAR} also exhibited seasonal variations, particularly in the middle- and high-latitude regions (Supplementary Note 1). In boreal regions, disparities in ρ_{PAR} and τ_{PAR} were reduced during summer because of higher CHL (Supplementary Note 1). In contrast, since CHL played a minor role in

the NIR region, its seasonality had little influence on the modeled ρ_{NIR} and τ_{NIR} (Supplementary Note 1). We also compared our PFC-based leaf ρ and τ to other LSMs[46–51,53]. Their PFT-based ρ_{PAR} and τ_{PAR} were generally similar to those in CLM, aligning with the lower bounds of the PFC-based estimates. Notably, CLASSIC[53] and JSBACH[50] scaled canopy albedo directly from leaf ρ, requiring lower leaf ρ to match other LSMs (Supplementary Note 1).

Surface energy budget

When implementing PFC-based LOP in CESM, the overall spatial patterns of surface PAR and NIR albedo did not show substantial differences (Supplementary Note 2). However, the PFC-based approach showed lower mean surface PAR and NIR albedo in tropical regions and higher surface albedo in boreal regions, with differences >0.05 (Fig. 2a, b). Similar patterns were found across CESM simulations following SSP245 and SSP585 (Supplementary Note 2). In the coupled simulations, CESM predicted slightly more variable albedo differences (e.g., lower surface albedo in some boreal forest regions; Supplementary Note 2); but the general patterns of higher boreal and lower tropical albedo persisted.

In regions where the surface albedo changed by >0.005 (otherwise no discernible impact was detected), the PFC-based annual mean PAR and NIR albedo agreed better with the MODIS MCD43C3 (v61) black sky albedo[59] in the tropics. Specifically, the mean PAR albedo bias decreased from− 50.1% to 16.2% and mean NIR albedo bias decreased from−78.5% to 62.8% from 23°S to 23°N (highlighted in cyan in Fig. 2c–f). However, in the boreal regions, the PFC-based annual mean albedo showed slightly worse agreement with MODIS MCD43C3 (mean
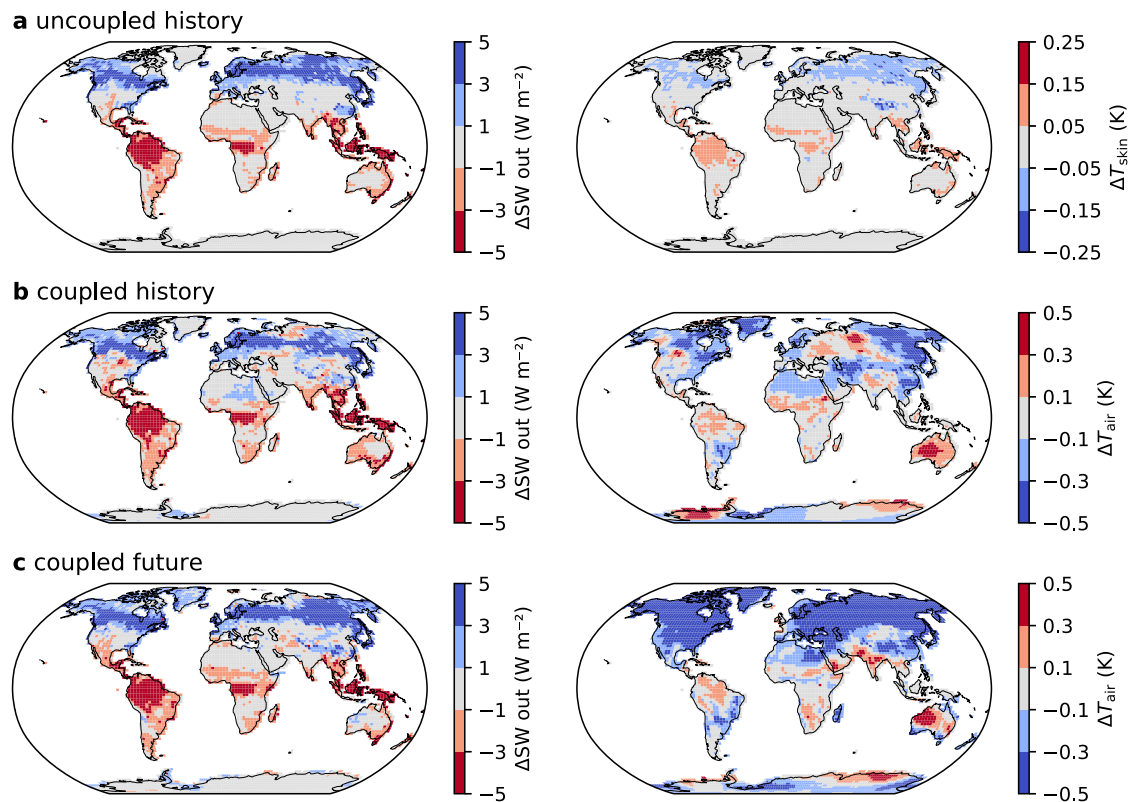
Fig. 3 | Changes in reflected shortwave radiation, skin temperature, and air temperature after accounting for the PFC-based leaf optical properties. **a** Simulation results for uncoupled historical simulations from 1985 to 2019. **b** Simulation results for the coupled run from 1950 to 2005. **c** Simulation results for the coupled run from 2015 to 2100. *Δ*SW out refers to the change in reflected

shortwave radiation at the last 20 years of the simulation period; *ΔT*$_{skin}$: change in skin temperature at the last 20 years of the simulation period; *ΔT*$_{air}$: change in air temperature at the last 20 years of the simulation period. Made with Nature Earth. Free vector and raster map data @ naturalearthdata.com.

PAR albedo bias increased from−34.5% to 48.2% and mean NIR albedo bias increased from− 70.6% – 85.1%; Fig. 2c–f). When comparing the albedo patterns on a monthly basis, we found overestimated PFC-based PAR and NIR albedo compared to MODIS MCD43C3 in the boreal regions from May to October (Supplementary Note 2), which led to the overall bias. The overestimated PFC-based PAR albedo in boreal regions suggested that CHL may be underestimated (Fig. 1a), while the overestimated PFC-based NIR albedo suggested that LMA or LWC may be underestimated (Fig. 1a). These results highlighted the importance of coupling spatial and temporal vegetation trait variations with biophysical properties in LSMs and ESMs.

On average, the tropical regions reflected less shortwave radiation and the boreal regions reflected more shortwave radiation after accounting for the PFC-based LOP; the difference was >5 W m^{-2}, meaning a >10 W m^{-2} biased daytime mean (Fig. 3; Supplementary Note 3). The changes in shortwave radiation led to compensating changes in sensible heat, latent heat, and longwave radiation (Supplementary Note 3). As air temperature was prescribed in the uncoupled mode (land only), the annual mean skin temperature increased by ~0.1 °C in the tropical regions while decreasing by about 0.1 °C in the boreal regions (Fig. 3a; Supplementary Note 3). Further, changes in the surface energy budget would propagate in the coupled land-atmosphere simulation given the impacts on the climatic variables (such as clouds, precipitation, and air temperature). Thus, in coupled land-atmosphere mode, as the sensible heat exchange between the canopy and the atmosphere was accounted for, the model predicted more variable air and skin temperature changes (e.g., >0.4 °C warmer in central Australia and >0.4 °C cooler in northeast Asia; Fig. 3b, c; Supplementary Note 3). For example, the Amazon rainforest was predicted to be about 0.1–0.2 °C warmer and Australia was predicted

to be about 0.1–0.5 °C warmer (Fig. 3b, c). The PFC-based simulations better agreed with the ECMWF (European Centre for Medium-Range Weather Forecasts) Reanalysis v5 (ERA5)[60], though simulation differences were about 10 times smaller than the dataset "bias" (assuming ERA5 reanalysis as the truth value; Supplementary Note 3). Compared to the spatial and temporal patterns of LOP changes, changes in spatial temperature showed opposite directions in many regions under the coupled land-atmosphere simulations (Fig. 3b, c; Supplementary Note 3). Notably, the middle- to high-latitude regions in the northern hemisphere were predicted to be colder than the PFT-based approach, further highlighting the need to model canopy optical properties and surface energy budgets more accurately, which is often overlooked in current developments of LSMs and ESMs.

Carbon cycle
Due to the increases in surface temperature, tropical regions were predicted to be less productive despite absorbing more radiation (Fig. 4; Supplementary Note 4). Reasons underpinning this trade-off included the higher leaf temperature and thus leaf-to-air vapor pressure deficit, and the decreased light availability in the lower canopy layers (due to lower leaf transmittance to PAR; Fig. 1c). In the uncoupled mode, leaf temperature exhibited minimal changes (<0.1 K; Fig. 3), and thus, the primary driver of gross primary productivity (GPP; higher value means higher productivity) differences was likely the altered vertical PAR profile within the canopy. For example, if ρ_{PAR} and τ_{PAR} decrease (similar to when CHL increases), upper canopy leaves absorb more PAR, while lower canopy leaves absorb less. Although the total canopy PAR absorption increases, upper canopy leaves are typically light-saturated, and the additional PAR does not enhance their photosynthesis. Reduced PAR availability in the lower canopy, where
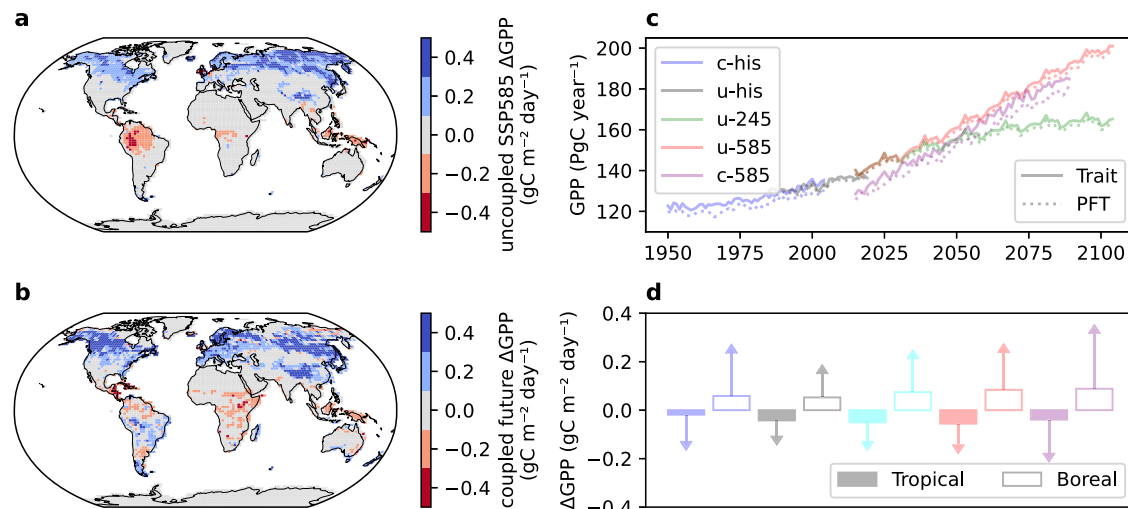
Fig. 4 | Changes in global carbon cycle after implementing PFC-based leaf optical properties. a Changes in gross primary productivity (ΔGPP; higher value for higher productivity) for uncoupled SSP585 simulations from 1985 to 2019. **b** ΔGPP for the coupled future run from 2015 to 2100. **c**, Time series of ΔGPP for various scenarios ("c-his" for coupled historical run, "u-his" for uncoupled historical run, "u-245" for uncoupled SSP245 run, "u-585" for uncoupled SSP585 run, and "c-585" for coupled SSP585 run). **d** ΔGPP of tropical (from 23°S to 23°N) and boreal (>50°S or >50°N) regions for various scenarios. The arrows plot the standard deviation of all grid cells. PFT plant functional type, PFC plant functional characteristic. Panels (**a** and **b**) made with Nature Earth. Free vector and raster map data @ naturalearthdata.com.

photosynthesis is often light-limited, can decrease overall GPP[61]. In contrast, though absorbing less solar radiation, the boreal forests were predicted to be a stronger carbon sink (Fig. 4; Supplementary Note 4). Reasons for the elevated photosynthesis included lower leaf temperature and thus leaf-to-air vapor pressure deficit, and the increased light availability in the lower canopy layers (due to higher leaf transmittance of PAR[61]; Fig. 1c).

Further, because of the higher magnitude and variation of changes in temperature under the coupled mode, changes in GPP also showed higher variations (Fig. 4). Overall, the PFC-based simulations suggested a slightly stronger land carbon sink, given the increased globally integrated GPP (Fig. 4c; Supplementary Note 4). When compared to a global GPP product trained from eddy covariance flux tower, remote sensing data, and machine learning[62], both PFT- and PFC-based GPP simulations agreed well with the reference data (Supplementary Note 4). However, no significant differences could be detected given that the magnitude of ΔGPP was 10-folder smaller than total GPP (Supplementary Note 4).

Cloud fraction and precipitation

Changes in the surface energy budget can propagate through the climate system, adding uncertainties in climate projections beyond those from internal variability. When vegetation absorbs more solar radiation, increased surface air and skin temperatures enhance global moisture cycling, leading to shifts in cloud formation and precipitation, further impacting the Earth's energy budget. Indeed, we found different climate projections for the simulation period of the coupled historical and future runs. For example, in the coupled future run, the mean cloud fraction and precipitation during the simulation period could differ by >3% and >250 mm year^{-1}, respectively (Fig. 5; Supplementary Note 5). Though dominated by surface-reflected shortwave radiation, the changes in cloud cover and surface/air temperatures propagated and impacted the top-of-atmosphere (TOA) outgoing radiation flux (Fig. 5b; Supplementary Note 5). At the monthly scale, for the coupled future run, the monthly mean cloud fraction could differ by >7%, the TOA outgoing radiation flux differed by >10 W m^{-2}, and the monthly cumulative precipitation could differ by >40 mm (Supplementary Note 5). On average, the Earth's outgoing radiation flux increased by 0.16 W m^{-2} during the coupled simulation

for the PFC-based configuration, although the globally integrated energy budget showed substantial interannual and seasonal variations (−3 to 3 W m^{-2} annually, and −5 to 6 W m^{-2} monthly; Supplementary Note 5).

Discussion

The evolution of state-of-art LSMs[46–53], corresponding to the "greening" of LSMs and ESMs[11], has mostly focused on improving representations of terrestrial carbon cycle processes, such as stomatal resistance, PFT distinctions, dynamic vegetation modeling, and cropland modeling[12]. In contrast, progress in improving the representation of surface energy fluxes in LSMs has lagged behind[14,15]. Despite substantial updates in hyperspectral RT models[22,23,29,63] and 3D ray-tracing RT models[28,64,65], these advances are not yet directly supported by ESMs given the demand for more computation resources and the lack of comprehensive model parameters. Addressing these limitations will advance ESM development, improve model representation of surface processes, and better harness the growing volume of remote sensing data for model calibration.

Indeed, when incorporating PFC-based LOP, which were derived from trait databases and remote sensing data, into CESM, we found potentially improved surface energy budgets, particularly in the tropics. Although the planetary energy budget tends to average out when integrated globally due to systematic differences between the PFT- and PFC-based surface albedo (i.e., the PFC-based approach has lower albedo in the tropics and higher albedo in boreal regions) (Supplementary Note 5), substantial regional differences could be identified in energy budgets, carbon fluxes, and climate projections. Recent work also demonstrated that land process uncertainty, particularly in surface fluxes such as albedo, can substantially impact the climatological mean state of temperature and precipitation through land-atmosphere coupling[66]. These findings highlight the value of improving the representation of canopy RT in ESMs and re-calibrating the model parameters under the new configuration, given that RT simulations influence multiple other coupled processes.

ESMs often have different configurations of key parameters like the response of plants to soil moisture[67] and the number and categories of PFTs in different LSMs[68]. Further, the look-up table values in these models have substantial differences even for the same PFT, such
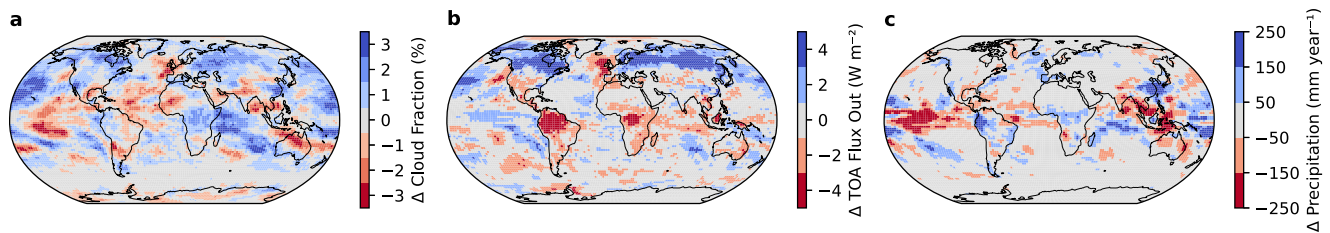
Fig. 5 | Changes in global climate projections for the coupled SSP585 run from 2015 to 2100. a Changes in annual mean cloud fraction (vertically integrated). **b** Changes in top-of-atmosphere (TOA) outgoing radiation flux (sum of shortwave and longwave radiation). **c** Changes in annual mean precipitation. All plotted results are averaged from the last 20 years of the simulation period. Made with Nature Earth. Free vector and raster map data @ naturalearthdata.com.

as the leaf level ρ and τ (Supplementary Note 1). For example, while LSMs have their ρ_{PAR} and τ_{PAR} close to or lower than the lower boundary predicted by the PFC-based approach, they differ more in their ρ_{NIR} and τ_{NIR} settings (Supplementary Note 1). Notably, three other LSMs (CoLM[46], JULES[48,49], and ORCHIDEE[47]) showed similar patterns as CLM in their PFT-based ρ_{NIR} values falling within or exceeding the PFC-based range, while their τ_{NIR} values falling within or lower than the PFC-based range (Supplementary Note 1). Therefore, we expect that implementing the PFC-based LOP into these LSMs would yield similar results as the CESM/CLM models used in this study. One exception is the CABLE model[51] with both lower ρ_{NIR} and τ_{NIR}, suggesting a generally lower NIR albedo than other LSMs. Superseding the PFT-based static look-up tables with the PFC-based configurations will help reduce the configuration-resulted differences among the LSMs and ESMs[68,69]. Yet, quantitatively and systematically evaluating the impacts of replacing the PFT-based approach with more trait-informed approaches would require more investigations, for example, adding surface albedo information and designing new experiments in the next phases of the Coupled Model Intercomparison Project (CMIP)[70,71] and TRENDY[72] would help accelerate this transition.

Accurately modeling the surface energy budget requires: (1) reliable LOP such as ρ and τ and background soil albedo in multiple spectral bands, (2) accurate canopy structural parameters such as leaf area index, clumping index, and leaf angle distributions[40,73–75], and (3) an appropriate canopy RT model that captures the interactions between radiation and vegetation. Currently, most LSMs employ simple broadband RT schemes developed in the 1980s[14,15] along with the PFT-based look-up table approach. While some recent work has examined the impact of foliar clumping[18] on energy fluxes, major limitations with the broadband RT model have not been addressed. For instance, the broadband leaf ρ and τ values depend not only on leaf biophysical traits and states such as CHL, LMA, and LWC[22], but also the spectral incident light (e.g., leaf absorbs less green light than blue and red light). Addressing these limitations would require RT models to move from broadband to higher spectral resolutions or to make corrections based on leaf and canopy optical characteristics[20]. In either case, more accurate observations and representations of plant traits and states are critical inputs to advance leaf and canopy RT models.

In the present study, we used globally gridded CHL[42] and LMA[37] to derive broadband leaf ρ and τ. We note here that, while the PFC-based LOP approach has substantial potential to better represent the spatial and temporal variations of vegetation diversity in comparison to the time-invariant PFT approach, these derived parameters still rely on the accuracy of the input parameters. To investigate the sensitivity of simulated surface albedo to different prescribed leaf trait inputs, we used CliMA Land to perform a series of simulations with varying combinations of CHL and LMA. Specifically, we tested a total of 14 combinations from two CHL datasets[42,76] and seven LMA datasets[37,38,77–81]. In each CHL and LMA combination, we simulated the hyperspectral surface albedo, calculated the mean broadband albedo over the relevant spectral ranges, and compared the results to MODIS albedo products[59]. Our results show a potentially improved PAR

albedo in the tropics across all tested combinations. However, improvements in NIR albedo were only observed in three out of seven LMA datasets (Supplementary Note 6). These findings highlight that the large uncertainties inherent in prescribed PFCs, such as CHL and LMA, can significantly influence the simulated surface energy budget and its coupled processes. In addition, the lack of seasonal variation in these prescribed traits likely introduces extra biases in model simulations, for example CHL[42] exhibits well-documented seasonality (Supplementary Note 2). LMA is also known to vary over time, since (1) leaves are built in a progressive manner from the beginning of a growing season, (2) plants tend to invest more in leaf mass under water-stressed conditions[82], (3) the relative contributions of different species to total leaf area can shift seasonally. Despite this knowledge, the lack of detailed and species-specific data on LMA seasonality and plant life history strategies precluded us from incorporating dynamic LMA fields into our simulations. We acknowledge this as a limitation and suggest that future work should prioritize the development of temporally resolved trait datasets to better capture these dynamics.

Besides CHL and LMA, many key plants traits or characteristics necessary for the leaf hyperspectral model are not typically directly measured. For example, the leaf mesophyll structural parameter (N) that partitions a leaf into N homogeneous layers was set to be a constant of 1.4 in our simulations, which is unrealistic for grasses with palisade mesophyll on both sides (i.e., $N > 2$ should be used for grass). LWC, which impacts NIR absorption[22,23], was assumed to be 5 mol m^{-2}, and a spatially and temporally resolved water content setting would further improve the accuracy in modeling vegetation RT. For example, when we changed the default LWC to 10 mol m^{-2}, ρ_{PAR} and τ_{PAR} showed minimal changes, but ρ_{NIR} and τ_{NIR} both decreased because of the NIR absorption by water (Supplementary Note 6). Moreover, leaf water dynamics could also impact leaf angle distribution and thus the light extinction coefficient within the canopy, particularly during a drought as the leaves may wilt and curl. Yet, to date, LSMs do not usually account for these impacts.

Further, vegetation traits exhibit pronounced phenological dynamics and may have asymmetric acclimation and stress responses to environmental conditions within a growing season (e.g., CHL[42,83]), as well as to the rapidly changing climate (e.g., species distributions and ranges[84]). In the present study, we prescribed CHL, LMA, leaf structural N, and LWC to derive global-scale LOP, aggregated them to annual means, and used the averages for all scenarios including the past and future. Despite the potential improvements in the tropics that have weaker seasonality, this simplification could introduce biases into the surface energy and carbon budgets, particularly for the regions with substantial seasonal variations such as in deciduous temperate forests. To address these limitations, future work should integrate physiological or empirical models that dynamically simulate vegetation acclimation to the environment, enabling the derivation of LOP in response to changing environmental conditions in real time. For example, we performed site-level simulations with CliMA Land, theorizing a dry-down experiment under four scenarios: (1) moderate CHL, moderate LMA, and constant LWC, (2) doubled CHL, moderate LMA, and

constant LWC, (3) moderate CHL, doubled LMA, and constant LWC, and (4) moderate CHL, moderate LMA, and dynamic LWC. While the general patterns of GPP and evapotranspiration (ET) remained largely unchanged, the outgoing shortwave radiation (sum of PAR and NIR) could differ >7 W m^{-2}, 28 W m^{-2}, and 3 W m^{-2} for the high CHL, high LMA, and dynamic LWC scenarios, respectively (Supplementary Note 6). These simulations further highlighted the importance of capturing temporal variations of vegetation characteristics in ESMs, which are typically overlooked. More research to quantify the spatial and temporal patterns of key plant traits or states (such as N, LMA, other leaf pigments, LWC) and their plasticity to climate variability is crucial for advancing ESMs configurations.

In addressing the role of LOP in ESMs, particularly their influence on temperature and key carbon cycle fluxes, it is crucial to consider the complexities introduced by canopy structure. Factors such as foliar clumping, leaf angle distribution, and the penumbra effect significantly influence the interception and scattering of solar radiation within forest canopies. These structural attributes are themselves affected by leaf size, shape, and spatial arrangement. For instance, leaf clumping can alter the effective leaf area index perceived by RT models, thus impacting simulations of photosynthesis, ET, and energy fluxes[17,18,73,74,85]. Similarly, the leaf angle distribution affects the directional reflectance of the canopy, which in turn influences the energy balance and microclimate[75]. Additionally, the penumbra effect, which refers to the shading patterns created by overlapping leaves, can lead to heterogeneity in light distribution, thereby affecting photosynthetic efficiency and thermal regulation within the canopy[86–88]. These factors may also co-vary with LOP and change with the environment. Future research therefore would benefit from the integration of detailed observations and modeling of canopy structure, in combination to the LOP. We note here that extra attention should be paid to the underlying assumptions and simplifications of different models, which could lead to inconsistencies that result in unexpected biases[89].

We envision that future ESMs would transit from PFT-based configurations to more process- and PFC-based configurations. Such shift would require numerous incremental quantitative changes, new schemes, and optimization of existing schemes. To make it easier for other LSMs to utilize the PFC-based LOP, our model output datasets are publicly available[90]. As the leaf reflectance and transmittance are globally gridded, integration of these PFC-based maps to other LSMs and ESMs should be readily applicable. For example, the function calls to read PFT from a given latitude and longitude, and then to read ρ and τ from the PFT can be redirected to a new function call, where ρ and τ are directly provided from the globally gridded maps. Further, with the advances in data science, remote sensing data, and retrieval techniques, more sophisticated vegetation characteristic maps will be available in the near future, helping curate new and more reliable datasets to feed LSMs and ESMs. For example, the recently launched and to-launch satellites with hyperspectral sensors such as EMIT[91], PACE[92], and SBG[93] missions could provide more spectral information about NIR reflectance that is sensitive to LMA and LWC, helping constrain these less studied vegetation characteristics.

In summary, we showed that accounting for the spatial and temporal variations in leaf biophysical traits can substantially impact the surface and TOA energy budgets, as well as estimates of the land carbon uptake−both modulating climate projections. Differences of >5 W m^{-2} in reflected shortwave radiation caused by underrepresented leaf trait diversity within PFTs underlines the need to further improve RT schemes and configurations in ESMs. Moving beyond simplified modeling approaches to more advanced model designs (e.g., from broadband to hyperspectral, from PFT- to PFC-based) in future-generation LSMs would allow for a more accurate representation of land surface process, and hence better leverage data to understand how these processes evolve over time[12]. Enhanced precision of climate projections would enable policymakers and scientists to develop more effective strategies for mitigating and adapting to climate change. These advances are essential for ensuring sustainable ecosystem management and achieving global climate goals.

Methods

Leaf optical properties

We ran global simulations with a spatial resolution of 2.5° × 1.875° (144 longitudes and 96 latitudes) following the procedure used in CESM. We obtained the CHL and LMA per grid cell using GriddingMachine.jl[94]. For LMA, we used the 0.5° × 0.5° dataset[37] as the primary data source and a secondary 0.5° × 0.5° dataset[38] to fill the missing points. For CHL, we used the weekly 0.5° × 0.5° dataset[42] and resampled the data to the monthly mean per grid. We then resampled the CHL and LMA maps to 2.5° × 1.875° using the Blender module from GriddingMachine.jl[94].

Per 2.5° × 1.875° grid, we derived the hyperspectral leaf reflectance and transmittance spectra using the LeafOptics.jl module from CliMA Land, which is adapted from the PROSPECT model[22,23,43,56]. The key leaf biophysical characteristics (trait or state) required are mesophyll structural parameter (N), leaf pigment constitutes (anthocyanin, brown pigments, chlorophyll, and carotenoid), LMA, and water content. Due to the limited data availability of these characteristics, we used a constant $N = 1.4$, anthocyanin content of 0, brown pigments content of 0, carotenoid content to be 1/7 of CHL[42], and a constant water content of 5 mol m^{-2} (equivalent to a thickness of 0.09 mm). Then, we computed the hyperspectral reflectance and transmittance, and used the average solar radiation spectrum $[E(\lambda)]$ to weigh the broadband leaf ρ and τ at PAR and NIR ranges:

$$\rho_{***} = \frac{\int_{\lambda_1}^{\lambda_2} E(\lambda) \cdot \rho(\lambda) \cdot \mathrm{d}\lambda}{\int_{\lambda_1}^{\lambda_2} E(\lambda) \cdot \mathrm{d}\lambda} \tag{1}$$

$$\tau_{***} = \frac{\int_{\lambda_1}^{\lambda_2} E(\lambda) \cdot \tau(\lambda) \cdot \mathrm{d}\lambda}{\int_{\lambda_1}^{\lambda_2} E(\lambda) \cdot \mathrm{d}\lambda} \tag{2}$$

where the subscript "***" means either PAR or NIR, and λ_1 and λ_2 the lower and upper bounds of the wavelength ranges of PAR (400−700 nm) and NIR (700−2500 nm). With the monthly broadband ρ and τ, we further computed the annual means.

CESM simulations

CESM2 is the most recent coupled ESM developed at the National Center for Atmospheric Research (NCAR) in partnership with universities and other research institutions[57]. Our global simulations were based on CESM 2.1, for which the atmosphere component is the Community Atmosphere Model (CAM) version 6, the land component is CLM version 5, the land ice component is the Community Ice Sheet Model (CISM) version 2, the ocean component is the Parallel Ocean Program (POP) version 2, the river runoff component is the Model for Scale Adaptive River Transport (MOSART), the sea ice component is Community Ice CodE (CICE) version 5, and the wave component is the WaveWatch version 3[52,57,95–97]. With the PFC-based annual means per grid, we modified CESM's land component CLM (version 5) to replace the PFT-based broadband leaf ρ and τ. We then ran the CESM using two branches of CLM: a default branch using the PFT-based look-up table values (control) and the modified CLM using the PFC-based values (treatment). We ran CESM with five setups: uncoupled historical run from 1985 to 2019 using the component set IHistClm50BgcCrop, uncoupled SSP245 scenario run from 2015 to 2104 using the component set ISSP245Clm50BgcCrop, uncoupled SSP585 scenario run from 2015 to 2104 using the component set ISSP585Clm50BgcCrop, coupled historical run from 1950 to 2004 using the component set FHIST_BGC, and coupled future run from 2015 to 2099 using the

component set BSSP585. We output monthly means per setup for analysis. We compared the results from 2015 to 2089 for the coupled future simulations.

Data availability

The CHL[42] and LMA[37,38] maps and benchmark datasets[62,98] used in this study are available from GriddingMachine.jl[94]. Global scale LOP maps derived using CliMA Land, CESM modifications, and CESM model output are available at https://doi.org/10.5281/zenodo.7570314[90].

Code availability

The CliMA Land model used to simulate leaf hyperspectral reflectance and transmittance is available at https://github.com/CliMA/Land. All figures were generated using Python with the matplotlib and cartopy modules. The code for generating and analyzing the data can be found at https://doi.org/10.5281/zenodo.7570314[90].

References

1. Seneviratne, S. I., Donat, M. G., Mueller, B. & Alexander, L. V. No pause in the increase of hot temperature extremes. *Nat. Clim. Change* **4**, 161–163 (2014).
2. Fischer, E. M. & Knutti, R. Anthropogenic contribution to global occurrence of heavy-precipitation and high-temperature extremes. *Nat. Clim. Change* **5**, 560–564 (2015).
3. Rumpf, S. B. et al. From white to green: Snow cover loss and increased vegetation productivity in the European Alps. *Science* **376**, 1119–1122 (2022).
4. Fowler, H. J. et al. Anthropogenic intensification of short-duration rainfall extremes. *Nat. Rev. Earth Environ.* **2**, 107–122 (2021).
5. Román-Palacios, C. & Wiens, J. J. Recent responses to climate change reveal the drivers of species extinction and survival. *Proc. Natl. Acad. Sci. USA* **117**, 4211–4217 (2020).
6. Liu, Z. et al. Challenges and opportunities for carbon neutrality in China. *Nat. Rev. Earth Environ.* **3**, 141–155 (2021).
7. Williams, J. H. et al. Carbon-neutral pathways for the United States. *AGU Adv.* **2**, e2020AV000284 (2021).
8. Lawrence, P. J. & Chase, T. N. Representing a new MODIS consistent land surface in the community land model (CLM 3.0). *J. Geophys. Res. Biogeosci.* **112**, G01023 (2007).
9. Friedlingstein, P. et al. Global carbon budget 2023. *Earth Syst. Sci. Data* **15**, 5301–5369 (2023).
10. Schlesinger, W. H. & Jasechko, S. Transpiration in the global water cycle. *Agric. For. Meteorol.* **189-190**, 115–117 (2014).
11. Pitman, A. J. The evolution of, and revolution in, land surface schemes designed for climate models. *Int. J. Climatol.* **23**, 479–510 (2003).
12. Fisher, R. A. & Koven, C. D. Perspectives on the future of land surface models and the challenges of representing complex terrestrial systems. *J. Adv. Model. Earth Syst.* **12**, e2018MS001453 (2020).
13. Braghiere, R. K. et al. Modeling global carbon costs of plant nitrogen and phosphorus acquisition. *J. Adv. Model. Earth Syst.* **14**, e2022MS003204 (2022).
14. Norman, J. M. Simulation of microclimates. In *Simulation of Microclimates* 65–99 (Elsevier, 1982).
15. Sellers, P. J. Canopy reflectance, photosynthesis and transpiration. *Int. J. Remote Sens.* **6**, 1335–1372 (1985).
16. Bonan, G. B. et al. Modeling canopy-induced turbulence in the Earth system: a unified parameterization of turbulent exchange within plant canopies and the roughness sublayer (CLM-ml v0). *Geosci. Model Dev.* **11**, 1467–1496 (2018).
17. Braghiere, R. K. et al. Accounting for canopy structure improves hyperspectral radiative transfer and sun-induced chlorophyll fluorescence representations in a new generation Earth system model. *Remote Sens. Environ.* **261**, 112497 (2021).
18. Li, F. et al. Vegetation clumping modulates global photosynthesis through adjusting canopy light environment. *Glob. Change Biol.* **29**, 731–746 (2023).
19. Braghiere, R. K. et al. The importance of hyperspectral soil albedo information for improving Earth system model projections. *AGU Adv.* **4**, e2023AV000910 (2023).
20. Wang, Y. & Frankenberg, C. Toward more accurate modeling of canopy radiative transfer and leaf electron transport in land surface modeling. *J. Adv. Model. Earth Syst.* **16**, e2023MS003992 (2024).
21. Wang, Y. et al. Beyond the visible: accounting for ultraviolet and far-red radiation in vegetation productivity and surface energy budgets. *Glob. Change Biol.* **30**, e17346 (2024).
22. Jacquemoud, S. & Baret, F. PROSPECT: A model of leaf optical properties spectra. *Remote Sens. Environ.* **34**, 75–91 (1990).
23. Féret, J.-B., Berger, K., De Boissieu, F. & Malenovský, Z. PROSPECT-PRO for estimating content of nitrogen-containing leaf proteins and other carbon-based constituents. *Remote Sens. Environ.* **252**, 112173 (2021).
24. Yao, Y. et al. Investigating diurnal and seasonal cycles of vegetation optical depth retrieved from GNSS signals in a broadleaf forest. *Geophys. Res. Lett.* **51**, e2023GL107121 (2024).
25. Anderegg, L. D. L. et al. Representing plant diversity in land models: an evolutionary approach to make "functional types" more functional. *Glob. Change Biol.* **28**, 2541–2554 (2022).
26. Cranko Page, J., Abramowitz, G., De Kauwe, M. G. & Pitman, A. J. Are plant functional types fit for purpose? *Geophys. Res. Lett.* **51**, e2023GL104962 (2024).
27. Bonan, G. B., Levis, S., Kergoat, L. & Oleson, K. W. Landscapes as patches of plant functional types: An integrating concept for climate and ecosystem models. *Glob. Biogeochem. Cycles* **16**, 5 (2002).
28. Gastellu-Etchegorry, J.-P. 3D modeling of satellite spectral images, radiation budget and energy budget of urban landscapes. *Meteorol. Atmos. Phys.* **102**, 187–207 (2008).
29. van der Tol, C., Verhoef, W., Timmermans, J., Verhoef, A. & Su, Z. An integrated model of soil-canopy spectral radiances, photosynthesis, fluorescence, temperature and energy balance. *Biogeosciences* **6**, 3109–3129 (2009).
30. Jiang, J., Comar, A., Weiss, M. & Baret, F. FASPECT: A model of leaf optical properties accounting for the differences between upper and lower faces. *Remote Sens. Environ.* **253**, 112205 (2021).
31. Sperry, J. S. et al. Pragmatic hydraulic theory predicts stomatal responses to climatic water deficits. *N. Phytol.* **212**, 577–589 (2016).
32. Sperry, J. S. et al. Predicting stomatal responses to the environment from the optimization of photosynthetic gain and hydraulic cost. *Plant, Cell Environ.* **40**, 816–830 (2017).
33. Kennedy, D. et al. Implementing plant hydraulics in the community land model, version 5. *J. Adv. Model. Earth Syst.* **11**, 485–513 (2019).
34. Wang, Y., Sperry, J. S., Anderegg, W. R. L., Venturas, M. D. & Trugman, A. T. A theoretical and empirical assessment of stomatal optimization modeling. *N. Phytol.* **227**, 311–325 (2020).
35. Wang, Y. & Frankenberg, C. Technical note: common ambiguities in plant hydraulics. *Biogeosciences* **19**, 4705–4714 (2022).
36. Kattge, J. et al. TRY - a global database of plant traits. *Glob. Change Biol.* **17**, 2905–2935 (2011).
37. Butler, E. E. et al. Mapping local and global variability in plant trait distributions. *Proc. Natl. Acad. Sci.* **114**, E10937–E10946 (2017).
38. Boonman, C. C. F. et al. Assessing the reliability of predicted plant trait distributions at the global scale. *Glob. Ecol. Biogeogr.* **29**, 1034–1051 (2020).
39. Kattge, J. et al. TRY plant trait database - enhanced coverage and open access. *Glob. Change Biol.* **26**, 119–188 (2020).
40. Yuan, H., Dai, Y., Xiao, Z., Ji, D. & Shangguan, W. Reprocessing the MODIS leaf area index products for land surface and climate modelling. *Remote Sens. Environ.* **115**, 1171–1187 (2011).

41. Wei, S., Fang, H., Schaaf, C. B., He, L. & Chen, J. M. Global 500 m clumping index product derived from MODIS BRDF data (2001-2017). *Remote Sens. Environ.* **232**, 111296 (2019).

42. Croft, H. et al. The global distribution of leaf chlorophyll content. *Remote Sens. Environ.* **236**, 111479 (2020).

43. Wang, Y. et al. Modeling global vegetation gross primary productivity, transpiration and hyperspectral canopy radiative transfer simultaneously using a next generation land surface model-CliMA Land. *J. Adv. Model. Earth Syst.* **15**, e2021MS002964 (2023).

44. Schneider, T., Lan, S., Stuart, A. & Teixeira, J. Earth system modeling 2.0: a blueprint for models that learn from observations and targeted high-resolution simulations. *Geophys. Res. Lett.* **44**, 12396–12417 (2017).

45. Bonan, G. B. & Doney, S. C. Climate, ecosystems, and planetary futures: the challenge to predict life in Earth system models. *Science* **359**, eaam8328 (2018).

46. Dai, Y. et al. The common land model. *Bull. Am. Meteorol.Soc.* **84**, 1013–1024 (2003).

47. Krinner, G. et al. A dynamic global vegetation model for studies of the coupled atmosphere-biosphere system. *Glob. Biogeochem. Cycles* **19**, GB1015 (2005).

48. Best, M. J. et al. The joint UK land environment simulator (JULES), model description - part 1: energy and water fluxes. *Geosci. Model Dev.* **4**, 677–699 (2011).

49. Clark, D. B. et al. The joint UK land environment simulator (JULES), model description - part 2: Carbon fluxes and vegetation dynamics. *Geosci. Model Dev.* **4**, 701–722 (2011).

50. Giorgetta, M. A. et al. Climate and carbon cycle changes from 1850 to 2100 in MPI-ESM simulations for the coupled model intercomparison project phase 5. *J. Adv. Model.Earth Syst.* **5**, 572–597 (2013).

51. Haverd, V. et al. A new version of the CABLE land surface model (Subversion revision r4601) incorporating land use and land cover change, woody vegetation demography, and a novel optimisation-based approach to plant coordination of photosynthesis. *Geosci. Model Dev.* **11**, 2995–3026 (2018).

52. Lawrence, D. M. et al. The community land model version 5: description of new features, benchmarking, and impact of forcing uncertainty. *J. Adv. Model. Earth Syst.* **11**, 4245–4287 (2019).

53. Melton, J. R. et al. CLASSIC v1.0: the open-source community successor to the Hcanadian land surface scheme (CLASS) and the canadian terrestrial ecosystem model (CTEM) - part 1: model framework and site-level performance. *Geosci. Model Dev.* **13**, 2825–2850 (2020).

54. Zhen, S. & Bugbee, B. Substituting far-red for traditionally defined photosynthetic photons results in equal canopy quantum yield for CO_2 fixation and increased photon capture during long-term studies: Implications for re-defining PAR. *Front. Plant Sci.* **11**, 581156 (2020).

55. Wright, I. J. et al. The worldwide leaf economics spectrum. *Nature* **428**, 821–827 (2004).

56. Wang, Y. et al. Testing stomatal models at the stand level in deciduous angiosperm and evergreen gymnosperm forests using CliMA Land (v0.1). *Geosci. Model Dev.* **14**, 6741–6763 (2021).

57. Danabasoglu, G. et al. The community Earth system model version 2 (CESM2). *J. Adv. Model. Earth Syst.* **12**, e2019MS001916 (2020).

58. O'Neill, B. C. et al. The scenario model intercomparison project (ScenarioMIP) for CMIP6. *Geosci. Model Dev.* **9**, 3461–3482 (2016).

59. Schaaf, C. & Wang, Z. *MODIS/Terra+Aqua BRDF/albedo albedo daily L3 global 0.05deg CMG v061.* https://data.nasa.gov/dataset/modis-terraaqua-brdf-albedo-albedo-daily-l3-global-0-05deg-cmg-v061-0cdb1 (2021).

60. Hersbach, H. et al. The ERA5 global reanalysis. *Q. J. R. Meteorol. Soc.* **146**, 1999–2049 (2020).

61. Wang, Y. & Yin, Y. Agriculture in silico: perspectives on radiative transfer optimization using vegetation modeling. *Crop Environ.* **2**, 175–183 (2023).

62. Tramontana, G. et al. Predicting carbon dioxide and energy fluxes across global FLUXNET sites with regression algorithms. *Biogeosciences* **13**, 4291–4313 (2016).

63. Yang, P., Verhoef, W. & van der Tol, C. The mSCOPE model: a simple adaptation to the SCOPE model to describe reflectance, fluorescence and photosynthesis of vertically heterogeneous canopies. *Remote Sens. Environ.* **201**, 1–11 (2017).

64. Bailey, B. et al. A scalable plant-resolving radiative transfer model based on optimized GPU ray tracing. *Agric. For. Meteorol.* **198-199**, 192–208 (2014).

65. Zhao, F. et al. FluorWPS: A Monte Carlo ray-tracing model to compute sun-induced chlorophyll fluorescence of three-dimensional canopy. *Remote Sens. Environ.* **187**, 385–399 (2016).

66. Zarakas, C. M. et al. Land processes can substantially impact the mean climate state. *Geophys. Res. Lett.* **51**, e2024GL108372 (2024).

67. Trugman, A. T., Medvigy, D., Mankin, J. S. & Anderegg, W. R. L. Soil moisture stress as a major driver of carbon cycle uncertainty. *Geophys. Res. Lett.* **45**, 6495–6503 (2018).

68. Arora, V. K. et al. Carbon-concentration and carbon-climate feedbacks in CMIP6 models and their comparison to CMIP5 models. *Biogeosciences* **17**, 4173–4222 (2020).

69. Arora, V. K. et al. Carbon-concentration and carbon-climate feedbacks in CMIP5 Earth system models. *J. Clim.* **26**, 5289–5314 (2013).

70. Eyring, V. et al. Overview of the coupled model intercomparison project phase 6 (CMIP6) experimental design and organization. *Geosci. Model Dev.* **9**, 1937–1958 (2016).

71. Stevens, B. A perspective on the future of CMIP. *AGU Adv.* **5**, e2023AV001086 (2024).

72. Sitch, S. et al. Trends and drivers of terrestrial sources and sinks of carbon dioxide: an overview of the TRENDY project. *Glob. Biogeoch. Cycles* **38**, e2024GB008102 (2024).

73. Pinty, B. et al. Simplifying the interaction of land surfaces with radiation for relating remote sensing products to climate models. *J. Geophys. Res.: Atmos.* **111**, D02116 (2006).

74. Chen, J. M. et al. Effects of foliage clumping on the estimation of global terrestrial gross primary productivity. *Glob. Biogeochem. Cycles* **26**, GB1019 (2012).

75. Yang, X. et al. Leaf angle as a leaf and canopy trait: rejuvenating its role in ecology with new technology. *Ecol. Lett.* **26**, 1005–1020 (2023).

76. Xu, M. et al. Retrieving global leaf chlorophyll content from MERIS data using a neural network method. *ISPRS J. Photogramm. Remote Sens.* **192**, 66–82 (2022).

77. Van Bodegom, P. M., Douma, J. C. & Verheijen, L. M. A fully traits-based approach to modeling global vegetation distribution. *Proc. Natl. Acad. Sci. USA* **111**, 13733–13738 (2014).

78. Madani, N. et al. Future global productivity will be affected by plant trait response to climate. *Sci. Rep.* **8**, 2870 (2018).

79. Moreno-Martínez, A. et al. A methodology to derive global maps of leaf traits using remote sensing and climate data. *Remote Sens. Environ.* **218**, 69–88 (2018).

80. Vallicrosa, H. et al. Global maps and factors driving forest foliar elemental composition: the importance of evolutionary history. *N. Phytol.* **233**, 169–181 (2022).

81. Schiller, C., Schmidtlein, S., Boonman, C., Moreno-Martínez, A. & Kattenborn, T. Deep learning and citizen science enable automated plant trait predictions from photographs. *Sci. Rep.* **11**, 16395 (2021).

82. Poorter, H., Niinemets, U., Poorter, L., Wright, I. J. & Villar, R. Causes and consequences of variation in leaf mass per area (LMA): a meta analysis. *N. Phytol.* **182**, 565–588 (2009).

83. Yu, L., Luo, X., Croft, H., Rogers, C. A. & Chen, J. M. Seasonal variation in the relationship between leaf chlorophyll content and photosynthetic capacity. *Plant, Cell Environ.* **47**, 3953–3965 (2024).

84. Austin, M. P. & Van Niel, K. P. Improving species distribution models for climate change studies: Variable selection and scale: species distribution models for climate change studies. *J. Biogeogr.* **38**, 1–8 (2011).

85. Braghiere, R. K., Quaife, T., Black, E., He, L. & Chen, J. M. Underestimation of global photosynthesis in Earth system models due to representation of vegetation structure. *Glob. Biogeochem. Cycles* **33**, 1358–1369 (2019).

86. Miller, E. E. & Norman, J. M. A sunfleck theory for plant canopies II. Penumbra effect: intensity distributions along sunfleck segments. *Agron. J.* **63**, 739–743 (1971).

87. Denholm, J. The influence of penumbra on canopy photosynthesis I. Theoretical considerations. *Agric. Meteorol.* **25**, 145–166 (1981).

88. Smith, W. K., Knapp, A. K. & Reiners, W. A. Penumbral effects on sunlight penetration in plant communities. *Ecology* **70**, 1603–1609 (1989).

89. Wang, Y. & Frankenberg, C. On the impact of canopy model complexity on simulated carbon, water, and solar-induced chlorophyll fluorescence fluxes. *Biogeosciences* **19**, 29–45 (2022).

90. Wang, Y. & Braghiere, R. Global scale leaf broadband optical properties derived from CliMA land and associated CESM simulations. *Zenodo* https://zenodo.org/records/15392827 (2024).

91. Green, R. O. et al. The Earth surface mineral dust source investigation: An Earth science imaging spectroscopy mission. In *2020 IEEE Aerospace Conference* 1–15 (IEEE, Big Sky, MT, USA, 2020).

92. Werdell, P. J. et al. The Plankton, Aerosol, Cloud, Ocean ecosystem mission: status, science, advances. *Bull. Am. Meteorol.l Soc.* **100**, 1775–1794 (2019).

93. Stavros, E. N. et al. Designing an observing system to study the surface biology and geology (SBG) of the Earth in the 2020s. *J. Geophys. Res. Biogeosci.* **128**, e2021JG006471 (2023).

94. Wang, Y. et al. GriddingMachine, a database and software for Earth system modeling at global and regional scales. *Sci. Data* **9**, 258 (2022).

95. Li, H. et al. A physically based runoff routing model for land surface and Earth system models. *J. Hydrometeorol.* **14**, 808–828 (2013).

96. van Werkhoven, B. et al. A distributed computing approach to improve the performance of the Parallel Ocean Program (v2.1). *Geosci. Model Dev.* **7**, 267–281 (2014).

97. Lipscomb, W. H. et al. Description and evaluation of the Community Ice Sheet Model (CISM) v2.1. *Geosci. Model Dev.* **12**, 387–424 (2019).

98. Jung, M. et al. The FLUXCOM ensemble of global land-atmosphere energy fluxes. *Sci. Data* **6**, 74 (2019).

Author contributions
Y.W. and R.K.B. planned and designed the research and led the writing. Y.W., R.K.B., W.W.F., Y.Y., Z.S., T.S., A.A.B., D.S., H.C., A.J.W., M.R., and C.F. analyzed the data and wrote the manuscript.

Competing interests
The authors declare no competing interests.

Additional information
Supplementary information The online version contains supplementary material available at https://doi.org/10.1038/s41467-025-60149-x.

Correspondence and requests for materials should be addressed to Yujie Wang.

Peer review information *Nature Communications* thanks Fa Li and the other, anonymous, reviewer for their contribution to the peer review of this work. A peer review file is available.

Reprints and permissions information is available at http://www.nature.com/reprints

Publisher's note Springer Nature remains neutral with regard to jurisdictional claims in published maps and institutional affiliations.